Nuclear Instruments and Methods in Physics Research A 350 (1994) 57–72
North-Holland

NUCLEAR
INSTRUMENTS
& METHODS
IN PHYSICS
RESEARCH
Section A

Beam tests and calibration of the H1 liquid argon calorimeter with electrons

H1 Calorimeter Group [1]

Received 13 April 1994

Results are presented on the energy calibration of the H1 liquid argon calorimeter modules with electrons from a test beam in the energy range of 3.7 GeV to 80 GeV. The method to determine the calibration for the H1 experiment from these measurements by the use of detailed simulations is described. Various systematic checks of this calibration are given. The calorimeter response is uniform in space within $\pm 1\%$ and linear with energy within $\pm 1\%$. An average energy resolution of about $11.5\%/\sqrt{E\,[\mathrm{GeV}]}$ is achieved.

1. Introduction

In 1992 the new storage ring HERA started its operation and since then e–p collisions were observed by the H1 detector. This detector [1] was designed to be well adapted to the requirements of the HERA physics program, which includes tests of the standard model up to high $Q^2 (\approx 10^5$ GeV$^2)$ and low x $(\approx 10^{-4})$ as well as searches for new physics. A main component of the H1 detector is the large liquid argon (LAr) calorimeter. The LAr technique was chosen, since it offers important advantages like good stability, ease of calibration, possibility of a fine segmentation and uniformity of the response. With these properties the physics requirements, especially a good measurement of the scattered electron, can be fulfilled. The precise measurement of the structure functions requires the absolute electromagnetic energy scale to be accurate on the 1% level, a relative electromagnetic energy resolution in the order of $10\%/\sqrt{E\,[\mathrm{GeV}]}$ and a well determined scattering angle [2].

In previous papers [4,5] we presented results on measurements performed in 1986–1987 at CERN, which served to optimize the calorimeter design. In this paper we report on test beam measurements at CERN with electrons using modules for the H1 LAr calorimeter. They were performed to verify the design goals of the calorimeter [3] and to determine the calibration constants for the various regions in the electromagnetic H1 LAr calorimeter.

The outline of the paper is as follows. In Section 2 the main features of the electromagnetic LAr calorimeter are described. In the third section the experimental set-up, data taking and simulation of the test beam measurements are discussed. The fourth section deals with corrections applied to the calorimeter charge signal. In the fifth section the calibration principle is described and results of systematic checks of the calibration procedure are presented. The sixth section summarizes results on the performance of the calorimeter.

Other properties of the H1 LAr calorimeter like the quality of the measurement of pions or the ability to separate electrons from pions are described in Refs. [6] and [7] respectively.

2. The electromagnetic liquid argon calorimeter of the H1 detector

In this section, the main features of the electromagnetic H1 LAr calorimeter are summarized. The calorimeter is described in Ref. [1] in the context of the H1 detector and in more detail in a separate paper [8].

Fig. 1 shows a vertical cut along the beam axis of the H1 LAr calorimeter. It consists of a fine grained electromagnetic part followed by a coarser hadronic part. Mechanically it is divided in the z-direction (see Fig. 1) in eight self-supporting wheels, named according to their position with respect to the proton beam: Inner Forward (IF), Outer Forward (OF), Forward Barrel (FB 1, 2), Central Barrel (CB 1, 2, 3) and Backward Barrel (BB). Adding the letter E to the abbreviations of the wheel names points to the electromagnetic part of the wheel.

In the azimuthal direction (ϕ), in the plane perpendicular to the z-axis, the wheels are separated either into two half rings (IF, OF) or into eight octants (FB, CB, BBE). These basic structures, called modules, are in the electromagnetic section built as a stack of absorber boards sepa-

[1] The members of the H1 Calorimeter Group are listed in the Appendix.

SSDI 0168-9002(94)00681-V

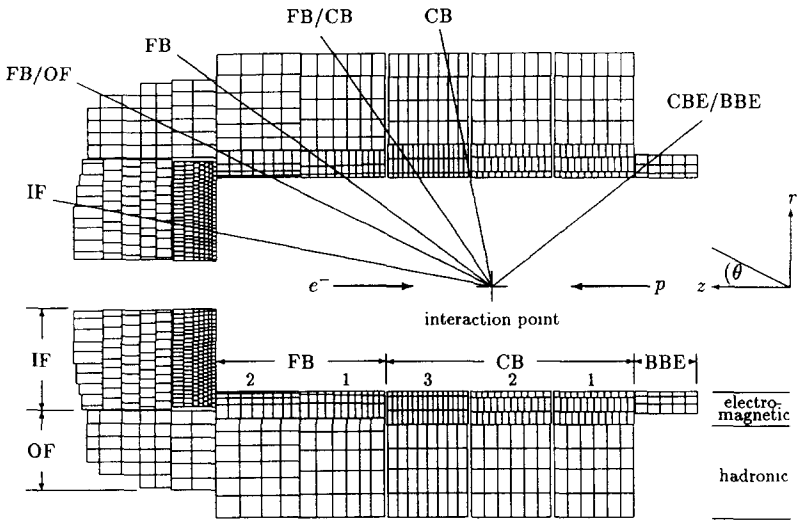

Fig. 1. Schematic view of the wheel and cell structure of the H1 LAr calorimeter. The lines from the interaction point indicate the nominal beam directions in the test set-up for the different calibration measurements discussed here. For spatial scans the beam was shifted perpendicular to the lines drawn in a way that the impact point of the particles moved either in the z-direction or perpendicular to the $r-z$-plane.

rated by layers of LAr. The absorber boards consist of a lead plate with copper cladded G10 plates glued on both sides. The mean values of the characteristic quantities for the electromagnetic section of the H1 LAr calorimeter are 1.6 cm for the radiation length X_0, 3.6 cm for the Molière radius R_M, 9.5 MeV for the critical energy ϵ_c and 30.5 cm for the interaction length λ_I. The read-out segmentation within a module depends on its position with respect to the proton direction. In the backward part it is coarse and it becomes finer moving to the forward direction. The longitudinal size of the cells increases from about 2.5 X_0 in the first r-segments (see Fig. 1), closest to the proton beam, to about 13 X_0 in the last r-segments. The lateral size of the cells varies between $1.0R_M$ in the forward region and about $2.5R_M$ in the backward region.

A schematic view of the basic sampling structure of the FBE wheel is given as an example in Fig. 2. The various wheels were produced with different techniques and the

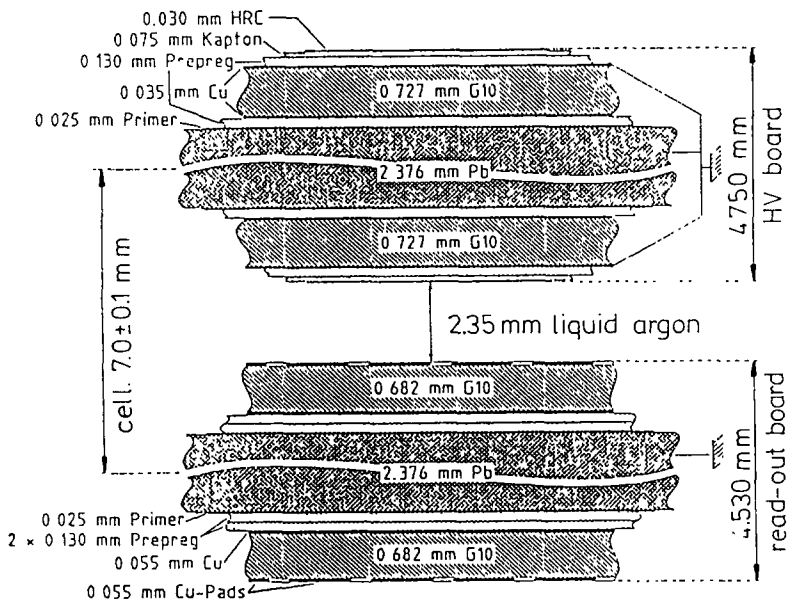

Fig. 2. Schematic view of the electromagnetic sampling structure in the FB2E wheel (not to scale).

exact thicknesses of the individual layers differ slightly. The LAr gap thickness is defined by spacers, which are glued between the boards in case of the CBE wheels or positioned by steel rods for the IFE, FBE and BBE wheels. In the CB region the absorber boards have to be oriented parallel to the beam direction, while in the other regions the orientation is perpendicular to it. Therefore different schemes were realized to hold the pile of boards together. Only the FBE module, shown in Fig. 3a, will be discussed in more detail, other modules having been produced along similar lines [8]. The effect of constructions for conserving the uniformity of the calorimeter response were studied by special measurements with a FBE module in the test beam and results are presented in Section 6.

To protect the FBE modules against torsion the boards are put into a steel frame. For the necessary stiffness an additional steel plate of 6 mm thickness had to be placed in the center of the module. The rods and the steel plates represent inhomogeneities in the calorimeter structure and add absorber material to the calorimeter. In compensation the front, center and backward steel plates (Fig. 3a) replace the lead-kernel of two consecutive absorber boards. The

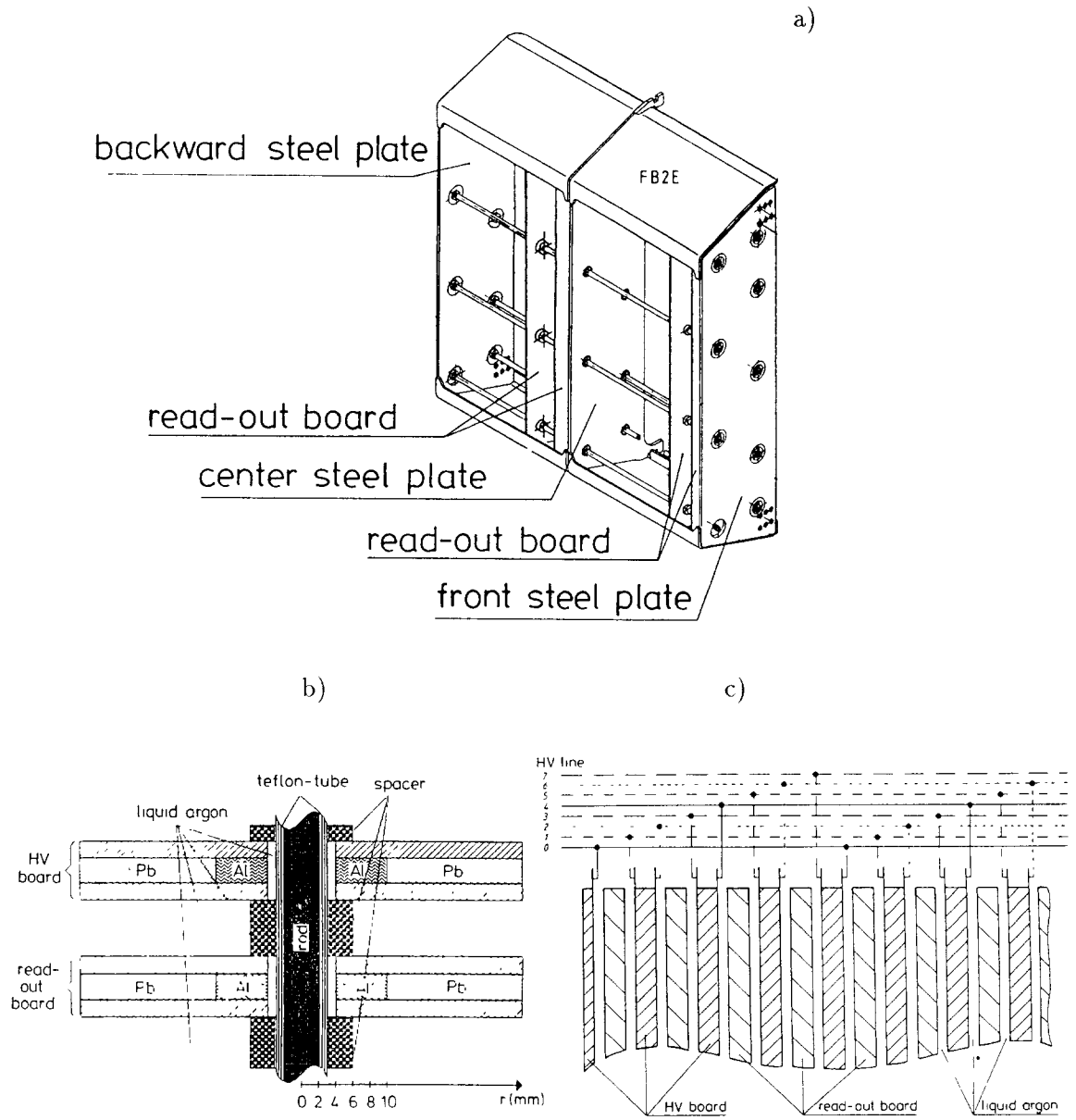

Fig. 3. Design characteristics of a FB2E module. (a) View of the support structure; (b) absorber board construction in the surrounding of the steel rods; (c) high voltage distribution.

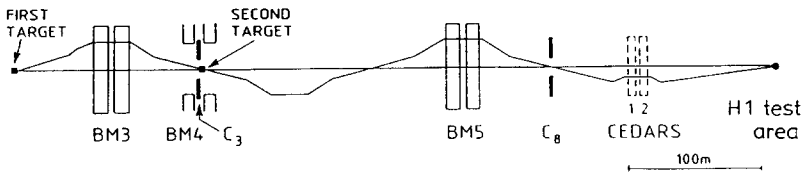

Fig. 4. Schematic view of the optics of the H6 beam in the vertical plane.

first board contains the steel plate and in the second one a thin G10-plate is the substitute for the lead-kernel. In the region of the rods the lead in the boards is replaced by an aluminum ring (Fig. 3b). The shower deposits there a smaller amount of energy and hence the energy loss in the steel rod can be compensated. The final layout of these constructions were optimized by simulations to reduce non-uniformities in the calorimeter response to the percent level [9,10].

To conserve the uniformity of the calorimeter signal in the case of a failure in the high voltage supply in the FBE and BBE modules, the high voltage distribution was optimized by simulations [9]. For example 8 HV supply-lines are available for each FB2E octant. Their distribution is shown in Fig. 3c. In case of a deteriorated line, the affected gaps with lower voltage are distributed over the full module. Results on special measurements, where the influence of one grounded high voltage line on the calorimeter response was studied, are discussed in the Section 6.

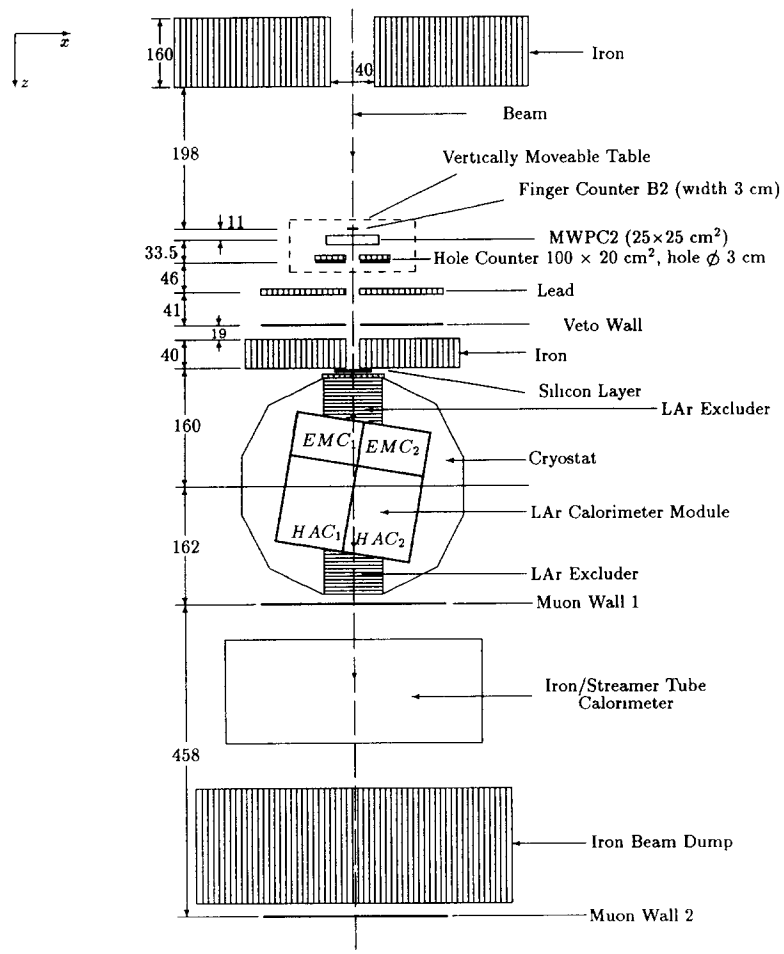

Fig. 5. Schematic view on the set-up in H1 test area at the H6 beam (dimensions in cm)

Table 1
Module configurations considered for the electromagnetic calibration of the H1 calorimeter. The polar angle θ is defined in Fig. 1

Configuration	Date	Mean angle θ	Ref.
FB1/FB2	July/Aug. 1989	34°	[12,13]
FB/CB	Sept. 1989	54°	[14]
CB	Oct. 1989	79°	[14]
IF	Nov./Dec. 1989	10°	[15]
	March 1990	dito	dito
CBE/BBE	April/May 1990	144°	[14,16]
FB/OF	June/July 1990	25°	[17,18]

3. Experimental set-up, data taking and simulation

The data were taken in a series of tests and calibration measurements with electrons, pions and muons from the H6 beam [11] at the CERN SPS for module configurations equivalent to the H1 detector. The calorimeter modules were arranged in the tests such that the angle of incidence for the central beam position corresponds to the angle of incidence in the geometry at HERA. The modules were either final modules, which were installed in the H1 wheels after the tests, or prototypes with the same constructional characteristics as the H1 modules. Since the calorimeter modules were produced with very strict mechanical constraints [8], they have a good uniformity. It is therefore sufficient to calibrate module combinations, which are typical for the H1 detector, rather than all the individual modules. Residual mechanical variations were carefully measured and recorded for each module during construction and can be corrected. The configurations of wheels tested are shown in Fig. 1, where the lines drawn indicate the nominal direction of the beam in the set-ups of the test measurements. Further details on the measurements considered in this paper can be found in the references given in Table 1.

3.1. The beamline

For all running periods the set-up of the H6 beamline [11] looked in principle like the one described in Ref. [4]. Most of the electron data were recorded by operating the beam in the so-called tertiary mode [19], which provides particle momenta up to 100 GeV/c. The beam optics is shown in Fig. 4. For the tertiary beam mode a secondary target built out of lead or polyethylene was introduced just behind the collimator C_3 in the bending magnet BM4. The momentum spread is defined by the adjustment of the collimators C_3 and C_8 and amounts to 0.5–0.8% in the given momentum range. The mean value of the beam momentum is known to $15\%/p$ [GeV] $\oplus$ 0.5% [2] (i.e. 0.7% at 30 GeV).

Between the differential Cherenkov counters (CEDAR) [21] and the cryostat, quadrupole magnets and the last vertical bending magnet BM9 are positioned allowing the trimming of the beam. These magnets are not shown in the figure. The vertical slope of the beam can be adjusted by the magnet BM9. This provides the possibility for vertical scans. Behind this magnet a 3 cm wide scintillation finger counter (B1) and a multi-wire proportional chamber (MWPC1) follow in the beamline. Two planes of scintillators are set up in front and behind the MWPC1. They give a trigger signal for the read-out of the MWPCs, whenever a beam particle hits both planes.

Further detectors defining the beam position and used for triggering are shown in Fig. 5, which gives a detailed overview of the experimental set-up in the H1 test area. A second scintillation finger counter (B2), turned by 90° with respect to the first one (B1), a second multi-wire proportional chamber (MWPC2) and a hole counter are placed on a vertically moveable table in order to define the beam position for vertical scans.

The accepted beam particles are limited by the two narrow finger counters to an area of 3×3 cm^2 and by the hole counter to a circle with a diameter of 3 cm. The two MWPCs, with two orthogonal wire planes each, allow the measurement of the horizontal and vertical position of the incident particle to a precision of 2 mm (FWHM). The typical horizontal and vertical beam widths amount to $\sigma \approx 0.8$ cm for the beam energies ≤ 10 GeV, shrinking to $\sigma \approx 0.3$ cm for higher energies ≤ 80 GeV.

Other trigger elements given in Fig. 5 are the veto wall and the two muon walls, which consist each of 10 scintillation counters 120 cm long and 20 cm wide. The front part of the veto wall is covered with 1 cm ($\approx 2\ X_0$) of lead to improve the sensitivity for low energetic photon rejection. The back side of the veto wall is shielded against the albedo of the calorimeter by an iron wall of 40 cm thickness. The iron/streamer tube calorimeter (used in Ref. [6]) was not analyzed for the electromagnetic showers considered for the calibration in this report.

The entrance window of the cryostat has a diameter of 60 cm. As mentioned before the magnet BM9 upstream bends the beam for vertical scans. Horizontal scans are possible by moving the cryostat. The useful diameter of the vessel is 250 cm and the maximum LAr height is around 190 cm. With these sizes the cryostat can house two complete H1 modules, both consisting of one electromagnetic (EMC_1) and one hadronic (HAC_1) section, as indicated in Fig. 5. A special module half of the standard transverse size had to be built only for the IF measurements.

Specially constructed argon excluders were put in front and behind the calorimeter modules in the cryostat to remove the inactive LAr in the beamline. This reduced the amount of inactive material in front of the calorimeters to a value between 1 and 1.5 X_0 depending on the set-up in the period, where the beamline itself contributes about 0.6 X_0 to the dead material in front of the calorimeter [20].

[2] N. Doble, private communication (1991)

The argon purity and the charge collection efficiency were monitored by three different methods. An overall monitoring was achieved by an oxygen-meter measuring the O_2-contamination continuously with sampled gas from the vapor phase of the argon. The second method exploits the charge collection efficiency determined with two α- and two β-probes, which are identical to those in the H1 detector and described in Refs. [1,8]. They were positioned very close to the calorimeter modules. The third method uses the calorimeter response to beam particles at different high voltage settings. This allows the measurement of the charge collection efficiency directly in the calorimeter modules. The results of the latter method and the corrections derived from it are discussed in Section 4.

3.2. Electronics and calibration

The front end electronics and calibration system were as close as possible to the H1 system at HERA, which is described in more detail in Refs. [1,8]. The analog signal processing chain for the calorimeter signals consists of a warm charge sensitive preamplifier and a shaping amplifier. The bipolar signals produced by the latter are strobed into a sample and hold unit upon trigger and fed into the analog read-out system after multiplexing by a factor 128. Two different gains are used to extend the dynamic range of a 12 bit ADC to 14 bit for half of the 2048 calorimeter channels available at the test experiment. The ADC data were read out by a fast CAB processor as described in Ref. [4]. No zero suppression nor data corrections were applied online. The corrections used in the offline analysis are discussed in Section 4.

The charge calibration of the read-out system is performed via capacitors of 47 pF in each read-out channel, which are charged by voltage pulses of known amplitude. The measured ADC signal is related to the injected charge by a third order polynomial, which allows the consideration of non-linearities in the analog–digital conversion. The overall precision of the calibration is dominated by timing shifts and amounts to 0.5% [22].

The stability of the read-out electronics depended mainly on temperature variations which made it necessary to calibrate at least once per day. Its quality was checked after every run by events in which all channels were pulsed at the same time. This check is also possible offline, since during the data taking a defined fraction of such events pulsed by the calibration system, were recorded besides the events triggered by beam particles.

The noise introduced by the read-out electronics corresponds on average to 3.5×10^4 electrons per read-out channel, equivalent to 20 MeV on the electromagnetic scale. Its value depends in the given range of cell sizes linearly on their detector capacitance. After pedestal correction the noise signals follow in good approximation a Gaussian distribution centered at zero.

3.3. Data taking

In addition to the events produced by real particles, calibration events mentioned above and random trigger events, where the trigger requires that no particle is in the calorimeter, were recorded. The latter are used to monitor the pedestal position and the electronic noise offline. They also provide a realistic description of the noise in simulated events by adding their signals to the simulated particle shower signals.

The following conditions had to be met by an event to be recorded and to be included in the analysis. A coincident signal of the two finger counters in anticoincidence with the hole counter and the veto wall define a beam particle. For the analysis it was required that both MWPCs should record a single cluster, to make sure both that the particle did not interact and start a shower in front of the calorimeter and that only one beam particle reached the calorimeter. In order to avoid pile-up of particle signals, events were accepted only if there was no second beam particle within 10 μs before or 3 μs after the event was triggered.

Particles were identified by the two CEDARs, which are filled with helium gas. Their pressure is adjustable such that the Cherenkov light produced by the selected particle type and momentum hits a ring of eight photomultipliers. At least one of the CEDARs had to fulfill a sixfold coincidence in its eight individual signals.

Four different types of data sets were recorded:

– stability runs: taken usually every day with the same impact position in the calorimeter and 30 GeV particles to monitor the time dependent decrease of the charge collection efficiency;

– HV-curve: taken at least at the beginning of the run period with 30 GeV particles at the same impact position as above. The applied high voltage was varied between 100 and 2800 V to determine the charge collection efficiency;

– uniformity scans: 30 GeV particles were used. The impact point in horizontal and vertical direction was varied systematically to explore the response of the calorimeter in special regions, e.g. in regions of cracks or rods;

– energy scans: data were taken with the same impact point for the particles as for the stability runs for different energies. These data allowed one to calibrate the calorimeter and to explore the linearity of its response.

For every run about 5000–10 000 events were recorded. After the trigger and particle identification cuts between a quarter to one half of the recorded events could be used in the analyses.

3.4. Simulation

Various program packages were used to simulate the measurements in the test beam. For calibration the standard H1 software with its GEANT 3.14 [23] framework

was modified by implementing the descriptions of the beamline geometry and all other special features of the experimental set-up. The simulation code contains a detailed description of the calorimeter geometry with LAr gaps separated from the absorber plates, consisting of a mixture of the lead kernel and the remaining material. The simulation also took into account the central position, the spatial width and the momentum spread of the beam. The shower particles were tracked down to an energy of 1 MeV for electrons and down to 0.2 MeV for photons. In special studies particles were followed down to an energy of 0.05 MeV. Recombination effects were taken into account according to Birks' law [24] with an effective energy deposition dE': $dE'/dx = (dE/dx)(1 + k_b dE/dx)^{-1}$, with the factor $k_b = 0.005$ g MeV^{-1} cm^{-2} (see Ref. [25]). In order to produce a realistic description of the electronic noise, each simulated event is overlaid by an experimental empty random trigger event.

For physics analysis H1 uses at present a faster simulation with parametrized electromagnetic showers as described in Ref. [26] (see Section 6, Fig. 16 for a result).

Special detailed simulations were performed with the EGS4 program [27] for the FBE and the BBE measurements [28,29] (see Section 6, Fig. 15 for results). Here the absorber plates were described as a lead kernel and a separate mixture of the remaining materials on both sides. The lowest energy for tracking electrons and positrons was set to 1.5 MeV and to 0.1 MeV for photons.

4. Corrections of the calorimeter signal

Some offline corrections to the recorded charge signal are necessary in order to remove the residual influences of the special experimental set-up at the test beam and to allow the transfer of the determined energy calibration to the H1 detector. The pedestal drift, the cross-talk between read-out channels and the slight variations of the capacitance of the calibration capacitors have been corrected. A further correction was performed concerning the LAr purity due to pollution of the LAr by calorimeter materials. The pollution is smaller in the H1 detector at HERA [8].

4.1. Effects due to electronics

The pedestals were determined during the electronics calibration separately for each channel. With the recorded random trigger events they can be checked and adjusted offline for each of the runs between two calibrations. The four calibration parameters describing the conversion function from ADC counts to measured charge are corrected offline to account for these new pedestals.

Capacitive couplings in the read-out chain cause a small cross-talk between channels, hence the measured charge is lower than the charge produced in the argon gap. The capacitive coupling is given by the design, in particular by the layout of the read-out lines on the read-out boards as shown in Ref. [16] or by the set-up of the experiment by insufficient shielding between read-out and calibration cables. During the standard calibration procedure all channels are pulsed simultaneously. Comparisons with pulsing each channel individually led to a correction function, parametrized by a third order polynomial, which takes into account the magnitude of the cross-talk as function of the ADC counts recorded [15]. The application of this cross-talk correction results in a $\leq 3\%$ increase of the reconstructed total charge in the calorimeter.

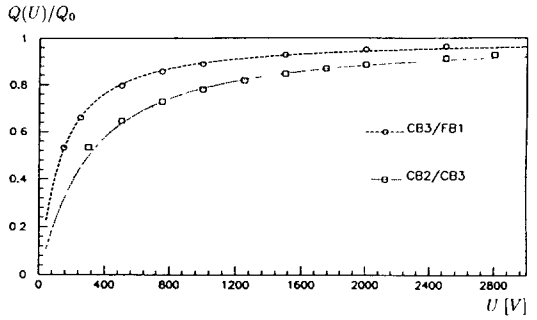

Fig. 6. Measured charge Q as function of the high voltage U applied to the calorimeters, normalized to the extrapolated plateau charge Q_0 for two different module configurations. The curves are fits based on Eq. (1).

The charge injection for the electronics calibration assumes coupling capacitors of 47 pF. Deviations from this value are considered by measuring the capacity of each capacitor separately and correcting the signal of each channel accordingly. The correction amounts to $\leq 0.8\%$ in the total reconstructed charge.

4.2. Influence of the purity

The correction of the influence of the LAr purity was done in two steps. At first the charge collection efficiency was determined at the beginning of the period by analyzing the HV-curve. In the second step the stability runs were analyzed and the time dependent decrease of the signal was parametrized by a straight line.

The HV-curves, as shown in Fig. 6 for two different periods, describe the measured charge as a function of the high voltage applied to the calorimeter. The dependence can be parametrized by the following equation [30]:

$$Q(|E|, P) = Q_0 2\frac{\lambda}{d}\left[1 - \frac{\lambda}{d}(1 - e^{-d/\lambda})\right], \qquad (1)$$

where Q_0 denotes the plateau charge. λ represents the mean free path length for a capture. It depends on the field strength and the impurity concentration P:

$$\lambda = \lambda(|E|, P) = \alpha\frac{|E|}{P}, \qquad (2)$$

with the field strength $|E| = U/d$, the applied high voltage U and the LAr gap width d. In Ref. [31] the proportional factor α was determined for oxygen impurities to 0.15 ± 0.03 [ppm cm^2/kV]. Assuming that the impurities are mainly caused by oxygen and that the other impurities can be described in oxygen-equivalents, the measured charge as a function of the applied field strength can be fitted with the help of Eq. (1) and (2). The charge collection efficiency is then given by the ratio of the measured charge at the nominal applied voltage and the fitted plateau charge Q_0. The statistical errors of this correction are very small in the case of our data. The systematic errors can be estimated using different parametrizations for the charge dependence on the applied field strength or by comparing the results with those of the probes. These comparisons lead to a systematic error of about 2.5% [14].

The second impurity correction eliminates the time dependent signal decrease caused by increasing argon impurities e.g. due to leaking security valves or permanent outgasing from materials inside the cryostat. Fig. 7 shows the decrease of the measured total charge produced by 30 GeV electrons during the measurements for the IF calorimeter module. Between the two periods the cryostat stayed closed and cooled for several weeks (note the strongly suppressed scale on the ordinate). A linear function is fitted to the measured signal decrease in this figure. With this function a correction factor was determined for each run corresponding to the time past since the beginning of the period and the recording of the run.

The determined charge collection efficiencies for the different configuration set-ups vary between 89.4% and 95.3%. The time dependent signal decrease was found to vary between 2% and 10% per month. These variations are mainly attributed to the use of different cleaning agents like alcohol, acetone or Frigen (Freon 12) used during the construction of the modules in the various participating institutes. In the H1 LAr calorimeter at HERA the charge collection efficiency was determined by the analysis of cosmic signals to 94.4% at an electric field value of 0.63 kV/mm [32]. The probes installed in H1 delivered a very small signal decrease with time of about 0.5% per year.

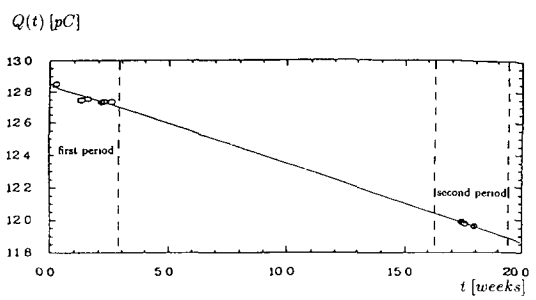

Fig. 7. Time dependent decrease of the measured charge Q for 30 GeV electrons during the time of the IF measurements, fitted by a straight line.

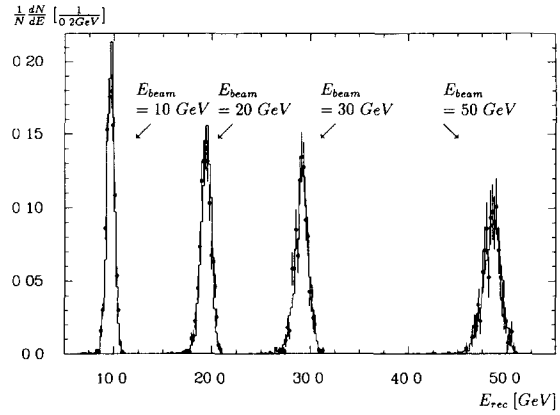

Fig. 8. Distribution of reconstructed energies E_{rec} for measured (histogram) and simulated (●) events in a BBE module for the beam energies 10, 20, 30 and 50 GeV.

The stronger decrease of the signal with time at CERN is attributed to flushing and cool-down procedures different to those used at HERA.

5. The electromagnetic energy scale and the absolute calibration

The applied calibration method aims to provide charge to energy conversion factors, which are independent of special conditions of the test beam measurements, that means independent of e.g. the inactive material in front of the calorimeters, energy leakages and noise suppression methods. The method used determines the charge-to-energy conversion within the active volume in the calorimeter modules by comparing the measured charge to the energy deposited in the calorimeter, calculated by detailed simulations [33]. This leads to an "ideal scale" (see Section 5.1 for its determination) which does not depend on noise suppression or detector imperfections. The size of the energy losses involved are visible in Fig. 8, where the distribution of the energy reconstructed on this scale are plotted for different beam energies. The signals follow a Gaussian distribution, note however that they are shifted towards lower energies in comparison to the beam energy. In the reconstruction program for events recorded with the H1 detector the energies are corrected for losses due to inactive material in front of the calorimeter and due to inactive spaces between modules (cracks) [1].

5.1. The determination of the calibration constants

The following three equations give a short-hand formulation of the calibration principle used to determine the set of calibration constants, one for each wheel type in the H1 calorimeter.

The energy is reconstructed from the measured charge according to:

$$E_{\mathrm{rec}}^{\mathrm{exp}} = c^{\mathrm{exp}} \sum_{i}^{\mathrm{channels}} Q_i. \tag{3}$$

The sum runs over the channels i with charges Q_i, which remain after application of cuts to suppress electronic noise. For the calibration data usually an asymmetric noise cut was applied, where only charges are considered, which are higher than a chosen multiple f of the standard deviation of the noise signals $Q_{\sigma,i}$ in the corresponding channel i:

$$Q_i > f Q_{\sigma,i}. \tag{4}$$

For the simulated events the energy is reconstructed by the following expression:

$$E_{\mathrm{rec}}^{\mathrm{sim}} = \sum_{j}^{\mathrm{channels}} \left\{ \left(c^{\mathrm{sim}} E_{\mathrm{vis},j} \right) + \left(c^{\mathrm{exp}} Q_{r,j} \right) \right\}. \tag{5}$$

The factor c^{sim} denotes the calibration constant for the simulated data which converts the visible energy $E_{\mathrm{vis},j}$ in the LAr into the energy deposited in the material of the corresponding calorimeter cell ($E_{\mathrm{dep},j}$). It is therefore the inverse sampling fraction of the calorimeter. This conversion factor has been determined by special simulations, where the electrons were introduced directly into the active volume of the calorimeters by averaging over the ratio of the total deposited and visible energies ($E_{\mathrm{dep}}/E_{\mathrm{vis}}$). The value of c^{sim} is dependent on the tracking cuts and granularity mode used in the simulations. Applying the c^{sim} belonging to the simulation mode the first part of Eq. (5) gives an estimate of the energy deposited in the calorimeter by the particle. The realistic electronic noise is added by the charges $Q_{\mathrm{r},j}$ from experimental random trigger events (see Section 3.3). Equivalent noise suppression cuts as for the data are applied to select the channels j in case of the simulated events. This procedure ensures that the influence of the noise and its suppression on the reconstruction of the deposited energy are identical for simulated and measured data. The equation

$$\left\langle E_{\mathrm{rec}}^{\mathrm{exp}} \right\rangle = \left\langle E_{\mathrm{rec}}^{\mathrm{sim}} \right\rangle \tag{6}$$

represents the condition for the determination of the experimental scale c^{exp}. This relation is fulfilled for all particle energies and for different schemes of noise suppression using a single calibration constant c^{exp} as demonstrated below.

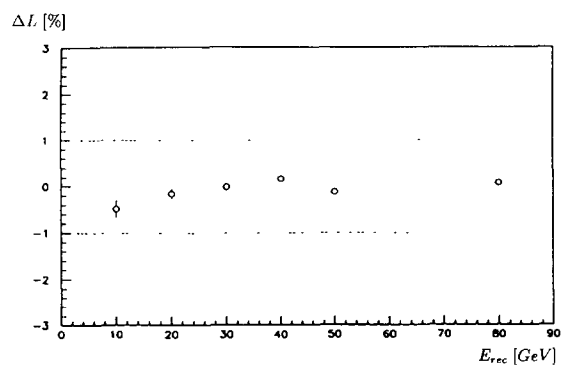

Fig. 9. Relative deviations ΔL between data and simulation (see Eq. (7)) as function of the beam energy E_{beam} for a CB3E module. The dotted lines mark the $\pm 1\%$ range.

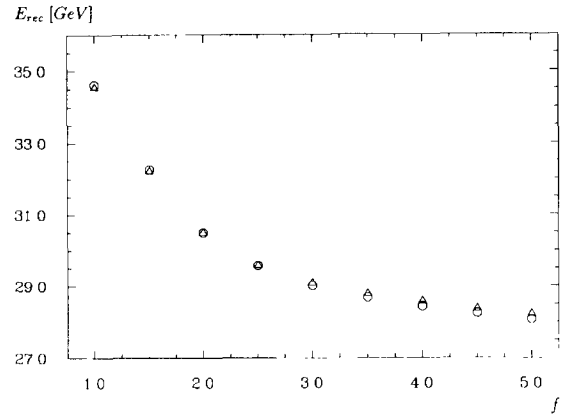

Fig. 10. Reconstructed energies as function of the noise threshold f (see Eq. (4) for definition) for measured (○) and simulated (△) events with 30 GeV electrons entering an IFE module. The statistical errors are smaller than the symbol size.

5.2. Systematic checks

Several studies were performed to check the quality of the determined calibration and the description of the modules by the simulations. Here the most important ones are mentioned:

a) Varying the particle energy. Fig. 8 demonstrates how well the measured energy distributions are reproduced by the simulations for electrons with different beam energies entering a BBE module. A more quantitative comparison is possible by defining the quantity ΔL:

$$\Delta L = \frac{E_{\mathrm{rec}}^{\mathrm{sim}} - E_{\mathrm{rec}}^{\mathrm{exp}}}{E_{\mathrm{rec}}^{\mathrm{exp}}}. \tag{7}$$

It denotes the relative deviation between the simulated and the measured data. This quantity is plotted in Fig. 9 for a fixed noise suppression for a CBE module. In this figure the relative deviations are below 0.5%.

b) Varying the noise suppression. The balance in Eq. (6) should be independent of the applied noise suppression scheme. The variation of the threshold for accepted charges according Eq. (4) by increasing the multiple f allows another systematic check. Fig. 10 shows the decrease of the reconstructed energy with increasing cut level f of the noise cut applied. The behavior is the same for measured and simulated data. The quantity ΔL is shown in Fig. 11

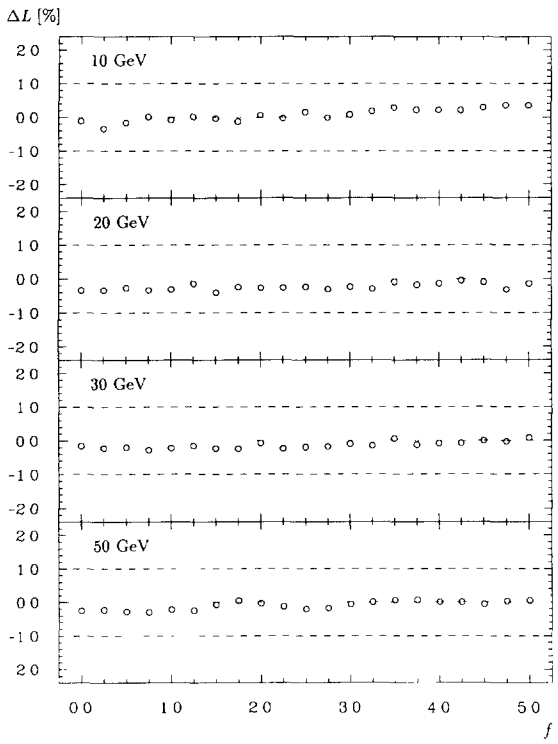

Fig. 11. Relative deviations ΔL (Eq. (7)) for various beam energies entering a BBE module as a function of the noise threshold f (Eq. (4)). The dashed lines mark the $\pm 1\%$ range. The statistical errors are smaller than the symbol size.

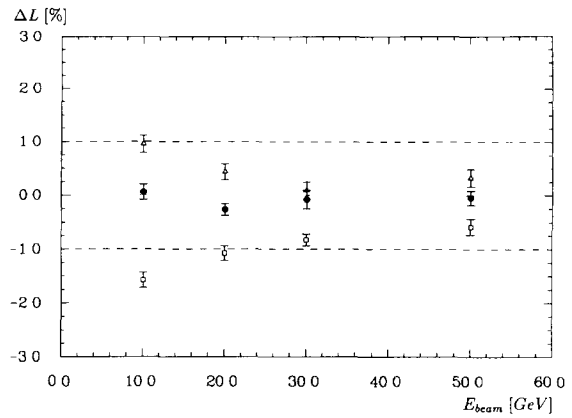

Fig. 12. Relative deviations ΔL (Eq. (7)) for various amounts of inactive material in front of the calorimeter (0.66 X_0 (Δ), 1.06 X_0 (●, nominal), 1.30 X_0 (□)) as a function of the energy of particles entering a BBE module. The dashed lines mark the $\pm 1\%$ range.

for several beam energies as a function of the noise threshold f. With careful adjustment of the inactive material in front of the calorimeter and of the impact point in the simulations by using shower profiles it was possible to restrict the relative deviations to $< 0.4\%$.

c) Sensitivity to the influence of inactive material in front. The quality of the simulation and its description of the geometry of the experimental set-up is clearly a crucial point for this method of calibration. To study the sensitivity to the material in front of the calorimeter, the amount of this material was set in the simulation to 0.66 X_0, 1.06 X_0 (the nominal value) and 1.30 X_0. Fig. 12 shows the influence of this large variation on the relative deviation in the reconstructed energy expressed by the quantity ΔL. The amount of inactive material in front of the calorimeter can be estimated independently of the calibration by comparing the longitudinal shower profiles for data and simulations with an accuracy of about 0.1 X_0 [16,18]. This is only a quarter to a third of the variations in the amount of inactive material in front of the calorimeter studied in Fig. 12. Therefore the uncertainty of the amount of inactive material in front of the calorimeter is negligible.

The sources contributing to the systematic error of the electromagnetic scale are collected in Table 2. The largest contribution to the uncertainty is due to the correction of the charge collection efficiency. The results from the correction method described in Section 4 agree on the level of 2.5% with those derived with the radioactive sources [14].

The smaller contributions (1%) from non-linearities and non-uniformities are discussed in Section 6. The uncertainty of the beam momentum contributes 0.7%, since the calibration constants were determined with 30 GeV electrons (Section 3.1). The thicknesses of the individual layers have very narrow production tolerances, which were measured during assembly of the modules. An uncertainty of about 0.5% follows from these measurements. The remaining sources contribute very little to the systematic uncertainty.

In summary a total systematic uncertainty of the electromagnetic scale of the order of 3% follows from the known error sources.

Table 2
Sources of the systematic errors with their estimated contributions

Source	Contributions
Beam momentum	0.7%
Electronic calibration	0.5%
Charge correction	0.4%
Charge collection efficiency	2.5%
Signal decrease with time	0.4%
Layer thicknesses	0.5%
Inactive material	0.2%
Uniformity	1.0%
Linearity	1.0%
Noise suppression	0.4%
Total	3.1%

5.3. Calibration constants for all wheel types

Table 3 summarizes the calibration constants for the calorimeter wheels determined by the data analysis. They are presently still used without change in the H1 calorimeter shower reconstruction program.

Since the different constructions of the calorimeter wheels are taken into account in the simulations the ratio of the experimental and the simulation scale should give a similar value for all wheels. This ratio:

$$\frac{c^{\mathrm{sim}}}{c^{\mathrm{exp}}} = \frac{E_{\mathrm{dep}}/E_{\mathrm{vis}}}{E_{\mathrm{dep}}/Q} = \frac{Q}{E_{\mathrm{vis}}}$$

represents the measured charge per visible energy in LAr. Its expected value can be calculated from the energy needed to produce an ion pair in LAr (23.6 eV [34]) and

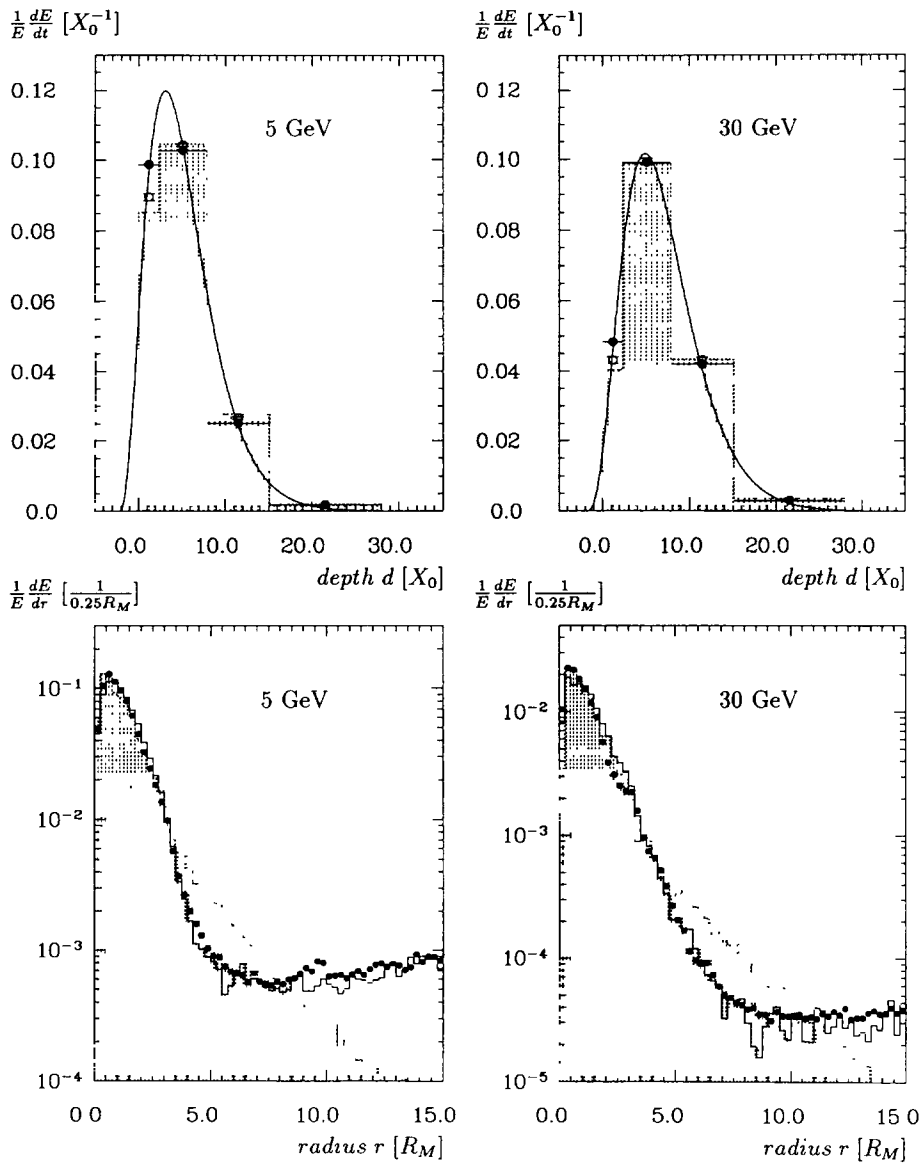

Fig. 13. Longitudinal (upper pictures) and lateral (lower pictures) shower profiles as reconstructed for 5 and 30 GeV electrons in the IFE calorimeter for data (●), GEANT simulations including noise (○ or histogram) and pure GEANT simulations (hatched histogram). The lines indicate fits to the longitudinal shower profiles.

Table 3
The electron calibration constants used for experimental (c^{exp}) and simulated (c^{sim}) signals for different wheels of the H1 LAr calorimeter. c^{sim} is the inverse of the sampling fraction for electromagnetic showers and therefore dimensionless

Calorimeter wheel	c^{exp} [GeV/pC]	c^{sim}	c^{sim}/c^{exp} [pC/GeV]
BBE	3.62	12.84	3.55
CBE	3.58	12.96	3.62
FBE	3.41	12.84	3.77
IFE	3.57	12.73	3.57

amounts to about 3.4 pC/GeV. The measured values in Table 3 differ slightly from the calculated expectation. The exact value for c^{sim} depends on the energy cut-offs for the tracking of the particles and the chosen granularity in the simulations. The simulations used for the results in Table 3 were all performed with the same cut-off and granularity choice. Therefore a common ratio c^{sim}/c^{exp} is expected for the different wheels. The determined values agree within 2.7% (rms), consistent with the estimated systematic uncertainty of 3.1% (Table 2).

Several tests are possible to check the electromagnetic energy scale used in the H1 analysis. One example is the study of electrons, which were generated by a cosmic muon traversing the H1 detector. By comparing the momentum measured in the tracker with the calorimeter response, the electromagnetic energy scale could be cross checked on the level of 3%. Further details on this procedure and other checks are discussed in Ref. [1].

6. Additional results from electron measurements

In this section results from the electron measurements in the test beam are presented, concerning the shower topology, the uniformity and linearity of the calorimeter response and the energy resolution.

6.1. Shower profiles

Fig. 13 shows the longitudinal and lateral shower profiles with respect to the reconstructed shower axis for two beam energies. They were measured in the IF calorimeter, which has the finest granularity among all H1 calorimeter wheels and which is, due to the approximately perpendicular impact direction, well suited for this measurement. The shower axis is reconstructed for each event by determining the impact point at the front face of the calorimeter and the center of gravity of the shower. In the longitudinal profiles the average relative energy deposit, normalized to the depth of each longitudinal segment, are shown as function of the calorimeter depth d. The lateral profiles are given by the average relative energy loss, integrated over the whole shower depth, as a function of the perpendicular distance radius r from the shower axis.

The data are compared with simulations performed with the GEANT program package. Both, the pure simulations and the simulations including overlaid noise combined with a noise suppression according to Eq. (4) with the cut level $f = 3$ are given. The measured data and the simulations with overlaid noise agree over two orders of magnitude. The longitudinal profiles were fitted with a standard parametrization given in Ref. [35] with the starting point of the showers and the normalization as free parameters. A good agreement is achieved. As can be seen in the lateral profile, the applied noise cut suppresses small shower signals at distances of 5–10 Molière radii (R_M), depending on the incident particle energy, while for distances $> 10R_M$, the contribution of noise to the reconstructed energy rises with r due to the increasing phase space.

6.2. Uniformity

The uniformity of the calorimeter response for different impact points of the particle depends not only on electronics effects like cross-talk, calibration or pedestal shifts, but also on mechanical inhomogeneities in the calorimeter caused by:
- production: e.g. thickness variations of the LAr gaps,
- construction: e.g. center plate out of steel, rods (Fig. 3) or z-cracks,
- hardware failures: e.g. shorts for a high voltage line.

The influence of these mechanical inhomogeneities are discussed in more detail in the following.

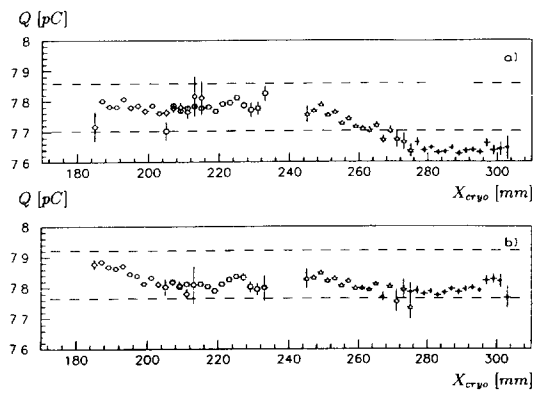

Fig. 14. Calorimeter signal in a scan, where the impact points of the beam particles moved in z-direction (see Fig. 1) across a FB2E module, without gap width correction (a) and with gap width correction (b). The center steel plate (see Section 2) is close to $X_{cryo} = 280$ mm. All data with the same symbol belong to one cryostat position, the real particle impact point was determined by using the MWPC2 (see Section 3.1). The dashed lines mark the $\pm 1\%$ range.

During the FB/OF calibration period special measurements were performed to study the effect of inhomogeneities in the FB2E module. Fig. 14 shows the reconstructed calorimeter signal from a scan, where the impact points of the beam particles moved in z-direction (see Fig. 1) across a FB2E module. The quantity X_{cryo} denotes the position of the cryostat. Taking into account the entrance angle of the particles into the calorimeter the variation of X_{cryo} by about 120 mm corresponds to a variation of 284 mm along the calorimeter surface. In Fig. 14b a correction for the variation of the gap width was applied according to the very detailed measurements performed during the assembly of the modules. Since the scan included the region of the steel plate in the center of the module, this figure demonstrates also that the compensation mechanism, discussed in the Section 2 works well. All variations of the calorimeter signal do not exceed the $\pm 1\%$ range as requested.

Another scan, where the impact points of the particles moved perpendicular to the r–z-plane (see Fig. 1) across a FB2E module, allows analyzing the influence of the spacer rods (see Section 2) on the calorimeter response. During the scan two rods were crossed. Without the compensating structure around the rods a signal decrease up to 13% in about 15% of the total calorimeter entrance area was predicted by simulation studies [10]. By means of the compensation mechanism (see Section 2) this percentage is reduced to about 3.0% with a maximal signal decrease of 3.5%. The upper part of Fig. 15 shows the result of the scan and in the lower part a detailed comparison with EGS4 simulations is given. The first rod is at $Y_{\mathrm{cryo}} = -110$ mm and the second one at $Y_{\mathrm{cryo}} = 120$ mm. At these positions the calorimeter signal exceeds the $\pm 1\%$ range only in a narrow interval.

Fig. 16 shows a scan with 30 GeV electrons crossing the z-crack between the wheels CB2 and CB3. Note that this is the z-crack with the most unfavourable angle of incidence (see Fig. 1). Shown are the response in the electromagnetic part only and the combined response including the hadronic section. The decrease of the signal is reproduced by the simulations with parametrized electromagnetic showers (see Section 3.4). This simulation was used to develop a correction for the H1 shower reconstruction program. Also for ϕ-cracks between the separate modules of each wheel energy losses are expected. In 1992 additional measurements were done in the test beam at CERN and forthcoming analyses will lead to an appropriate correction for these energy losses.

A further possible deterioration of the uniformity is given by failures in the high voltage supply. In Section 2 the layout of the high voltage distribution for a FB2E module was discussed and shown in Fig. 3. It is optimized to conserve the uniformity of the calorimeter signal on the full module, such that a first order correction of losses due to a shortened high voltage line is obtained by simply multiplying with a factor given by the distribution of the

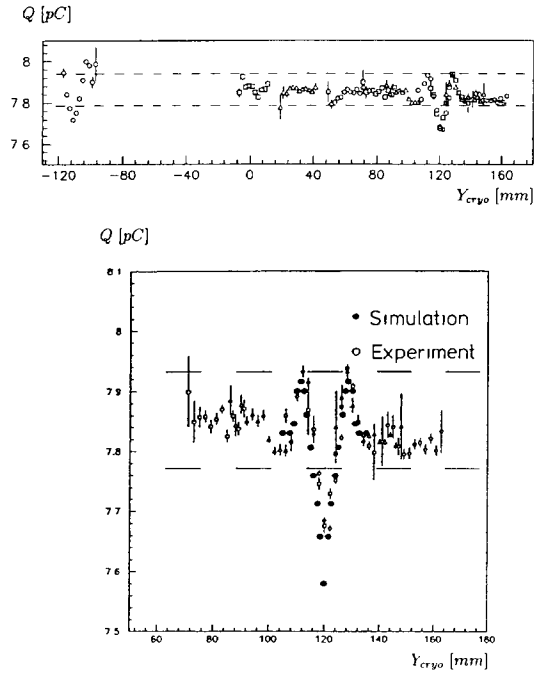

Fig. 15. Calorimeter signal of a FB2E module in a scan, where the impact points of the beam particles moved perpendicular to the $r-z$-plane (see Fig. 1) across a FB2E module. The upper picture shows the whole scan with the crossing of two rods ($Y_{\mathrm{cryo}} = -110$ mm, $Y_{\mathrm{cryo}} = 120$ mm). All data with the same symbol belong to one beam setting with the bending magnet BM9, the real particle impact point was determined by using the MWPC2 (see Section 3.1). The lower picture shows a comparison with EGS4 simulations in the surrounding of the second rod. The dashed lines mark the $\pm 1\%$ range.

lines. The result of a special scan with one grounded high voltage line is presented in Fig. 17. The calorimeter response depends on the impact point. It is low if the shower maximum coincides with a grounded gap and maximal if the shower maximum is fully read out, in Fig. 17 around $X_{\mathrm{cryo}} = 164$ mm and 184 mm. Including the worst case, where the shower maximum covers a grounded gap, the signal stays within the $\pm 1\%$ range.

6.3. Linearity

In the experimental set-up inactive material was present in front of the calorimeter (see Section 5.2). Therefore, in order to check the linearity of the response in the regular calorimeter structure, the measured charge is not directly compared to the beam energy of the particles but to the energy deposited in the calorimeter module, which can be determined by detailed GEANT simulations. In Fig. 18 the deposited energy divided by the measured charge is plotted for different beam energies. To suppress noise both quantities were reconstructed in a fiducial volume of a FB2E module containing the complete shower. No additional noise treatment was applied in this analysis. This is justi-

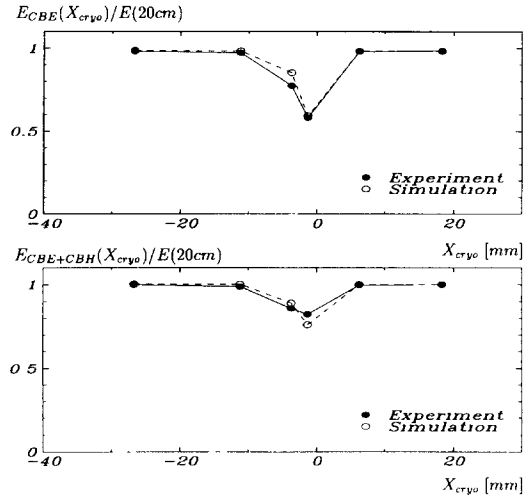

Fig. 16. Calorimeter signal of 30 GeV electrons in a scan across the most unfavourable z-crack between the CB2 and the CB3 modules (see Fig. 1). The upper picture shows the energy reconstructed in the electromagnetic module, while in the lower picture also the energy deposition in the hadronic part is considered. The reconstructed energies are normalized and compared with the energy measured at a distance of 20 cm from the crack (E(20 cm)). The simulation, based on parametrized electromagnetic showers (see Section 3.4), gives a good description of the data and was used to develop a correction for the H1 shower reconstruction program.

fied since the noise signals follow a Gaussian distribution and therefore the positive and negative noise contributions cancel in the mean value. The deviations from the linearity, showing up in Fig. 18, are limited to the $\pm 1\%$ range, marked with dashed lines. The fact that the low particle energies were produced by a special beam set-up and therefore measured in a separate time slice of the FB/OF period may explain the systematic shift to higher values. In addition the uncertainty of the mean beam momentum increases according to Section 3.1 up to 4.1% at the lowest particle energy 3.7 GeV.

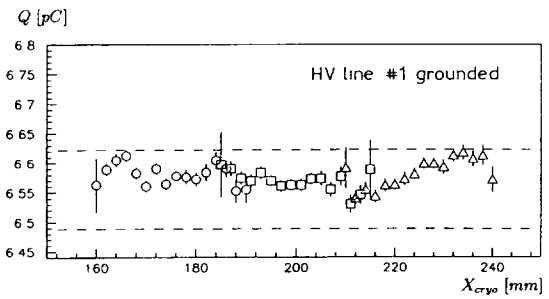

Fig. 17. Calorimeter signal in a scan measured in a FB2E module with one grounded high voltage line. All data with the same symbol belong to one cryostat position, the real particle impact point was determined by using the MWPC2 (see Section 3.1). The dashed lines mark the $\pm 1\%$ range.

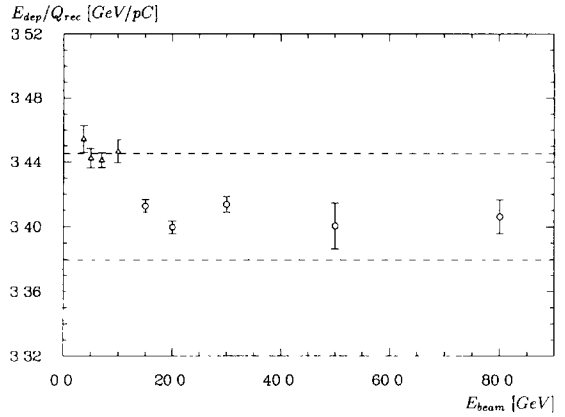

Fig. 18. Linearity of the calorimeter signal in a FB2E module as measured by the ratio of deposited energy, calculated by simulations, and reconstructed charge as a function of the beam energy. The values for $E_{\text{beam}} \leq 10$ GeV ($\triangle$) have been measured by a different set-up of the beam. The dashed lines mark the $\pm 1\%$ range.

The quantity ΔL, as defined in Eq. (7) and shown in Fig. 9 for a CBE module, respectively in Fig. 11 for a BBE module, is equivalent to the linearity discussed here, as the calorimeter is intrinsically linear in simulations. For all calorimeter modules the quantity ΔL is within $\pm 1\%$.

6.4. Energy resolution

The relative energy resolution $\sigma(E)/E$ as measured for the different calorimeter modules is plotted in Fig. 19 as a function of the beam energy. The dependence on the particle energy can be described by the function:

$$\frac{\sigma(E)}{E} = \sqrt{\frac{a^2}{E} + \frac{b^2}{E^2} + c^2}, \tag{8}$$

where the parameter a takes into account the intrinsic and sampling fluctuations and b the noise contribution. A

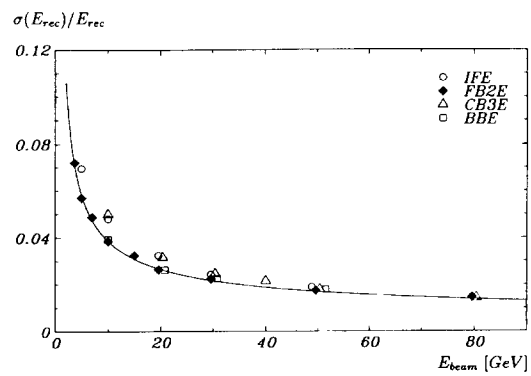

Fig. 19. Energy resolution for the various calorimeter wheels as a function of the beam energy.

Table 4
The parameters in the description of the relative energy resolution according to function (8) for the various calorimeter

Calorimeter wheel	Parameters		
	a [$\sqrt{\text{GeV}}$]	b [MeV]	c
BBE	0.094 ± 0.011	229 ± 41	0.011 ± 0.003
CBE	0.120 ± 0.002	325 ± 7	0.004 ± 0.001
FBE	0.112 ± 0.005	151 ± 4	0.006 ± 0.001
IFE	0.133 ± 0.002	200 ± 15	0.000 ± 0.005

constant term c arises from the intercalibration of the individual calorimeter channels and the momentum spread of the test beam of maximal 0.8% (see Section 3.1). Table 4 summarizes the values of the parameters, determined by a fit of the function (8) to the data of the various calorimeter modules. The slight differences are mainly due to the varying degree of noise suppression (2σ-, 3σ- or fiducial volume cut) chosen in each of the analyses and to the different amount of inactive material in front of the calorimeters for each of the set-ups.

7. Conclusions

Results have been presented on the performance of modules of the H1 LAr calorimeter in electron test beams.

The main goal of the measurements, in which the calorimeter response to electrons with an energy between 3.7 GeV and 80 GeV was analyzed, was the determination of the absolute electromagnetic calibration constants for the various calorimeter modules in the H1 detector. A method to extract the absolute calibration from these measurements using detailed simulations is described. The systematic uncertainty in the absolute scale amounts presently to about 3%. The set of calibration constants have been transferred to the H1 detector and checks of the electromagnetic scale in the final set-up at HERA verify the results obtained.

With the analysis of special measurements it could be shown that the total calorimeter response within a wheel is uniform within $\pm 1\%$ over almost all volumes.

The deviations from linearity are limited to $\pm 1\%$ and the energy resolution amounts to about $11.5\%/\sqrt{E\ \text{GeV}}$ on average.

Because of very tight construction tolerances which were achieved, the design goals for the calorimeter parameters were reached, thus satisfying most of the requirements of HERA physics.

Acknowledgements

We appreciate the big efforts of all the technical collaborators who constructed and maintained the calorimeters. The support of the CERN staff operating the SPS, the H6 beam line and the computer facilities is gratefully acknowledged. We thank all funding agencies for financial support.

Appendix

H1 Calorimeter group

B. Andrieu [10], J. Bán [6], E. Barrelet [11], G. Bernardi [11], M. Besançon [4], E. Binder [5], H. Blume [8], K. Borras [3], V. Boudry [10], F. Brasse [5], V. Brisson [9], A.J. Campbell [5], T. Carli [8], M. Colombo [3], Ch. Coutures [4], G. Cozzika [4], M. David [4], L. DelBuono [11], B. Delcourt [9], M. Devel [9], P. Dingus [10], A. Drescher [3], J. Duboc [11], R. Ebbinghaus [3], S. Egli [14], J. Feltesse [4], Y. Feng [11], W. Flauger [5,†], M. Flieser [8], K. Gamerdinger [8], J. Gayler [5], L. Goerlich [2], M. Goldberg [11], R. Grässler [1], H. Greif [8], M. Haguenauer [10], L. Hajduk [2], O. Hamon [11], P. Hartz [3], R. Haydar [9], W. Hildesheim [11], N. Huot [11], M.-A. Jabiol [4], A. Jacholkowska [9], M. Jaffre [9], H. Jung [1], C. Kiesling [8], Th. Kirchhoff [5], H. Kolanoski [3], V. Korbel [5], M. Korn [3], W. Krasny [2,4], J.P. Kubenka [8], H. Küster [5], J. Kurzhöfer [3], J.-F. Laporte [4], U. Lenhardt [3], P. Loch [5], D. Lüers [8,†], J. Marks [5], J. Martyniak [2], T. Merz [5], A. Nau [5], H.K. Nguyen [11], H. Oberlack [8], U. Obrock [3], C. Pascaud [9], S. Peters [8], H.B. Pyo [5], K. Rauschnabel [3], P. Ribarics [8], M. Rietz [1], V. Rusinov [7], N. Sahlmann [1], E. Sánchez [8], P. Schacht [8], V. Shekelyan [7,5], Y. Sirois [10], P. Staroba [12], H. Steiner [11], U. Straumann [14], J. Turnau [2], L. Urban [8], C. Vallée [11], M. Vecko [10], P. Verrecchia [4], Villet [4], D. Wegener [3], H.-P. Wellisch [8], T.P. Yiou [11], J. Žáček [9,13], Ch. Zeitnitz [5], F. Zomer [9]

[1] III. Physikalisches Institut der RWTH, Aachen, Germany [a].
[2] Institute for Nuclear Physics, Cracow, Poland.
[3] Institut für Physik, Universität Dortmund, Dortmund, Germany [a].
[4] DAPNIA, Centre d'Etudes de Saclay, Gif-sur-Yvette, France.
[5] DESY, Hamburg, Germany [a].
[6] Institute of Experimental Physics, Slovak Academy of Sciences, Košice, Slovak Republic.
[7] Institute for Theoretical and Experimental Physics, Moscow, Russian Federation.
[8] Max-Planck-Institut für Physik, München, Germany [a].
[9] LAL, Université Paris-Sud, IN2P3-CNRS, Orsay, France.
[10] LPNHE, Ecole Polytechnique, IN2P3-CNRS, Palaiseau, France.
[11] LPNHE, Universités Paris VI and VII, IN2P3-CNRS, Paris, France.
[12] Institute of Physics, Czech Academy of Sciences, Praha, Czech Republic.
[13] Nuclear Center, Charles University, Praha, Czech Republic.

[14] Physik-Institut der Universität Zürich, Zürich, Switzerland [b].
[†] Deceased.

[a] Supported by the Bundesministerium für Forschung und Technologie, FRG, under contract numbers 6AC47P, 6DO57I, 6MP17I respectively.
[b] Supported by the Swiss National Science Foundation.

References

[1] H1 Collaboration, The H1-Detector at HERA, DESY preprint 93–103 (1993).
[2] J. Feltesse, Proc. HERA Workshop, DESY, October 1987, ed. R.D. Peccei, Vol. 1, p. 33.
[3] H1 Collaboration, Technical Proposal for the H1 Detector, DESY (1986).
[4] H1 Calorimeter Group, W. Braunschweig et al., Nucl. Instr. and Meth. A 265 (1988) 419; Nucl. Instr. and Meth. A 275 (1989) 246.
[5] H1 Calorimeter Group, W. Braunschweig et al., Results from Test of a Pb-Fe Liquid Argon Calorimeter, DESY preprint 89-022 (1989).
[6] H1 Calorimeter Group, B. Andrieu et al., Nucl. Instr. and Meth. A 336 (1993) 499.
[7] H1 Calorimeter Group, B. Andrieu et al., Nucl. Instr. and Meth. A 344 (1994) 492.
[8] H1 Calorimeter Group, B. Andrieu et al., Nucl. Instr. and Meth. A 336 (1993) 460.
[9] K. Borras, Diploma Thesis, University of Dortmund (1987).
[10] U. Lenhardt, Diploma Thesis, University of Dortmund (1989).
[11] H6 Beam Tuning, CERN preprint, SPS/EPB/PC (1981).
[12] R. Grässler, Diploma Thesis, RWTH Aachen (1991).
[13] E. Sánchez, H1-internal report, H1-07/92-232 (1992).
[14] J.-F. Laporte, Thesis, University of Paris-Sud (1991); and H1-internal report, H1-04/92-218 (1992).
[15] P. Loch, DESY FH1K-92-02, Thesis, University of Hamburg (1992).
[16] K. Borras, Thesis, University of Dortmund (1992).
[17] M. Flieser, MPI-Phe/92-08, Diploma Thesis, Technical University of München (1992).
[18] P. Hartz, Thesis, University of Dortmund (1993).
[19] P. Coet, CERN/SPS 85-14 (1985).
[20] M. Kubantsev and V. Rusinov, Survey of the Experimental Set-Up after the July'88 running, H1-internal note (1988).
[21] C. Bovet et al., CERN/SPS/ 82-13 (1982).
[22] C. Pascaud et al., H1-internal report, H1-04/92-222 (1992).
[23] R. Brun et al., CERN DD/EE/84-1 (1987).
[24] J.B. Birks, Proc. Phys. Soc. 64 (1951) 874.
[25] C.W. Fabjan et al., Nucl. Instr. and Meth. 141 (1977) 61; J. Brau and T.A. Gabriel Nucl. Instr. and Meth. A 238 (1985) 489.
[26] S. Peters, MPI-PhE/92-13, Thesis, University of Hamburg (1992).
[27] R.L. Ford and W.R. Nelson, SLAC-Report 210 (1978); SLAC-Report 265 (1985).
[28] D. Guzik, Diploma Thesis, University of Dortmund (1991).
[29] U. Obrock, Diploma Thesis, University of Dortmund (1991).
[30] R. Hilsch and R.W. Pohl, Z. Phys. 108 (1937) 55.
[31] W. Hofmann et al., Nucl. Instr. and Meth. 135 (1976) 151.
[32] J. Stier, DESY FH1K-92-04, Diploma Thesis, University of Hamburg (1992).
[33] J. Gayler, H. Küster and P. Loch, H1-internal report, H1-04/91-171 (1991).
[34] M. Miyajima et al., Phys. Rev. A 9 (1974) 1439.
[35] Particle Data Group, Review of Particle Properties Phys. Lett. B 204 (1988).